


Article

Towards Binder Jetting and Sintering of AZ91 Magnesium Powder

Mojtaba Salehi ^{1,*} , Kai Xiang Kuah ², Jia Hern Ho ³, Su Xia Zhang ¹, Hang Li Seet ¹ and Mui Ling Sharon Nai ¹

- ¹ Additive Manufacturing Division, Singapore Institute of Manufacturing Technology (SIMTech), Agency for Science, Technology and Research (A*STAR), 2 Fusionopolis Way, Singapore 138634, Singapore
- ² Department of Materials Science and Engineering, National University of Singapore, 9 Engineering Drive 1, Singapore 117575, Singapore
- ³ School of Mechanical and Aerospace Engineering, Nanyang Technological University, 50 Nanyang Avenue, Singapore 639798, Singapore
- * Correspondence: mojtaba_salehi@simtech.a-star.edu.sg

Abstract: The inherent properties of magnesium (Mg) make it one of the most challenging metals to process with additive manufacturing (AM), especially with fusion-based techniques. Binder jetting is a two-step AM method in which green Mg objects print near room temperature, then the as-printed green object sinters at a high temperature. Thus far, a limited number of studies have been reported on the binder jetting of Mg powder. This study aimed to push the knowledge base of binder jetting and sintering for AZ91D powder. To this end, the principle of capillary-mediated binderless printing was used to determine the ink saturation level (SL) required for the binder jetting of a green AZ91 object. The effects of various SLs on forming interparticle bridges between AZ91 powder particles and the dimensional accuracy of the resultant as-printed objects were investigated. Green AZ91 objects sintered at different temperatures ranging from 530 °C to 575 °C showed a marginal increment in density with an increase in sintering temperature (i.e., 1.5% to 5.1%). The root cause of such a low sintering densification rate in the presence of up to 54.5 vol. % liquid phase was discussed in the context of the powder packing density of as-printed objects and swelling occurring at sintering temperatures ≥ 45 °C. Overall, this work demonstrates the great potential of binderless printing for AM of Mg powder and the need for pushing sintering boundaries for further densification of as-printed Mg components.



Citation: Salehi, M.; Kuah, K.X.; Ho, J.H.; Zhang, S.X.; Seet, H.L.; Nai, M.L.S. Towards Binder Jetting and Sintering of AZ91 Magnesium Powder. *Crystals* **2023**, *13*, 286. <https://doi.org/10.3390/cryst13020286>

Academic Editors: Xingrui Chen, Weitao Jia, Xuan Liu and Qiyang Tan

Received: 18 January 2023
Revised: 2 February 2023
Accepted: 6 February 2023
Published: 7 February 2023



Copyright: © 2023 by the authors. Licensee MDPI, Basel, Switzerland. This article is an open access article distributed under the terms and conditions of the Creative Commons Attribution (CC BY) license (<https://creativecommons.org/licenses/by/4.0/>).

Keywords: magnesium; binder jetting; additive manufacturing; binderless 3D printing; sintering

1. Introduction

Magnesium (Mg) is known to be the lightest structural metal and is gaining the attention of engineers and scientists as a promising candidate for designing lightweight components and structures. In AZ91 Mg alloy, aluminum and zinc are the principal alloying elements, with a content of 9 wt. % and 1 wt. %, respectively. The inclusion of aluminum significantly improves the corrosion resistance of AZ91, which has one of the lowest corrosion rates among commercially available Mg alloys [1]. In addition, AZ91 possesses good mechanical properties and castability, making it the most widely used Mg alloy for die-cast applications [2]. AZ91 can also be manufactured via various conventional techniques such as powder metallurgy and rolling [3].

Additive manufacturing (AM) technologies are increasingly used for processing Mg alloys. The Mg-AM techniques include binder jetting, laser powder bed fusion, material extrusion, wire and arc, and indirect 3D printing. The latest state-of-the-art study on research activities about AM of Mg alloys was reviewed by Zeng et al. [4]. The literature review and material portfolios of leading AM companies revealed that the technology readiness level for Mg alloys is still significantly behind other metals such as stainless steel, titanium, aluminum, and nickel-based superalloys. This stems from Mg's inherent characteristics, such as vigorous vapor pressure, high affinity for oxygen, a narrow processing window

(i.e., the melting point is close to the boiling point), and a stable oxide film covering Mg powder. To push Mg-AM boundaries, some aspects to consider for exploring the emerging knowledge base include: (i) protocols for safety, handling, storage, and recycling of fine Mg powder; ii) design and modification of AM techniques and machines; iii) development and optimizations of alloys and powders.

The laser powder bed fusion method dominates the AM of AZ91. There has been significant advancement in the AM field for AZ91. The combination of relentless efforts by researchers saw the overcoming of challenges that were once thought to be significant hurdles within only a short span of 6 years, such as the inadequate mechanical properties of the selective laser-melted AZ91 reported by Schmid et al. [5] in 2016 to the superior balance of strength and ductility reported in the work of Li et al. [6] in 2022. However, very few studies have reported developing other AM techniques for AZ91, such as the wire-and-arc method to develop thin-walled components [7], material extrusion to print the AZ91 feedstock for metal injection molding [8], and binder jetting followed by a complete liquid phase sintering process to densify small cylindrical-shaped samples [9]. More investigations into developing AM processes are therefore needed to advance the AM of AZ91.

Binder jetting is classified as a sinter-based AM technology, along with material extrusion, material jetting, and vat photopolymerization. While fusion-based AM allows for a single-step transformation of raw materials into manufactured parts, binder jetting first binds the powder in a desired geometry to form a green component, followed by a secondary step to debind and sinter the green component to form the manufactured parts. Binder jetting is known for its lower equipment cost, wider material choices, and enabling pieces to be stacked up during the build process [10,11]. We have developed an ex situ binder-free method based on the capillary-mediated assembly of Mg powder for the binder jetting of Mg-Zn-Zr and pure Mg powder [12,13]. These investigations were followed by advancing sintering strategies to densify as-printed specimens [14,15], developing surface coating methods [16], and characterizing the corrosion performance of differently sintered samples [17,18].

The present study aimed to develop the binder jetting and sintering of AZ91 powder. Firstly, green objects made from AZ91 powder were binder-jet printed at various ink saturation levels. The printability of AZ91 powder was assessed in terms of the shape fidelity and chemical composition of as-printed objects as well as the principles of capillary-mediated binderless printing. Secondly, the effects of sintering temperature and time on the macrostructure, microstructure, and density of as-printed AZ91 objects were thoroughly investigated.

2. Materials and Methods

2.1. Raw Powder

Mg alloy powder with the measured composition of Mg- 8.79 wt. % Al- 0.46 wt. % Zn- 0.17 wt. % Mn- 0.05 wt. % Si was supplied from the International Laboratory, USA. These elemental percentages fall within the allowable thresholds for AZ91D. Based on ASTM B212-13 and ASTM B527-15, the apparent and tap density of the Mg alloy powder were determined. Three repetitions of the procedure were performed to ensure consistency in measurements. The apparent and tap density of the powder were determined to be 0.9413 ± 0.0833 g/cm³ and 1.195 ± 0.0161 g/cm³, respectively. The AccuPYc II 1340 helium gas pycnometer was used to measure the density of the as-received powder. The pycnometer density was measured at 1.8872 ± 0.0009 g/cm³. The particle size distribution of the powder was determined from a laser particle scanner (Horiba LA-960). Figure 1a shows a Gaussian particle size distribution with D10 at 23.7 μm, D50 at 39.8 μm, and D90 at 61.8 μm. This is supported by the SEM of the powder in Figure 1b.

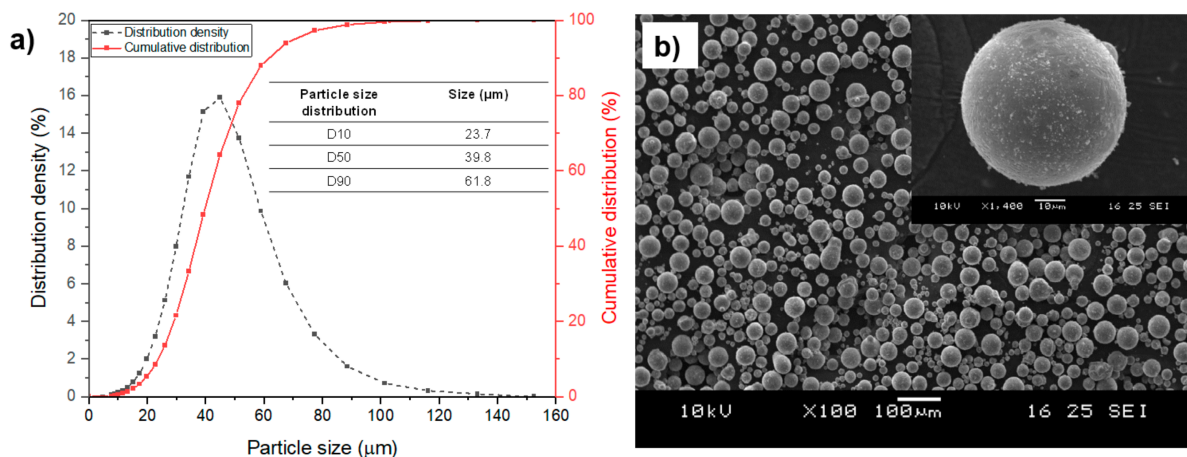


Figure 1. Characterization of the as-received AZ91 powder. (a) Particle size distribution obtained via laser light scattering and (b) SEM micrographs.

2.2. Binder Jetting

Figure 2 displays the capillary-mediated binderless 3D printing method developed in our earlier works to fabricate green Mg specimens [12,13,15]. The AZ91 powder was used as the powder feedstock of an in-house modified inkjet printer. Under ambient conditions (38 °C), an automated roller first spread a layer of powder (~100 μm) from the feed platform onto the build platform (Figure 2a). Then, the printhead deposited a formulated ink at a predetermined saturation level (SL) onto the build platform based on a sliced CAD design of objects. The SL in this work varied from 70% to 130%. Facilitated by the deposited ink and the capillary effect, solid interparticle bridges formed between particles, producing a layer of a green object (Figure 2b). The subsequent layer was spread on the previous one, followed by the selective deposition of the ink (Figure 2c), whereby solid interparticle bridges were created throughout the intralayer as well as the interlayer (Figure 2d). This layer-by-layer spreading of new powder rolling, ink deposition, and interparticle bridge formation was repeated until the desired green object was fully fabricated.

Multiple samples with various sizes and shapes, including cylinders of diameter 15 mm and length 60 mm and cubes of sides of 15 mm, were printed. When the overall printing cycle was completed, the build platform containing the green objects was left untouched for an hour to allow the ink to dry completely and the solid interparticle bridges to evolve. Afterward, the green objects were retrieved from the powder bed and prepared for sintering.

2.3. Sintering

Differential scanning calorimetry (DSC) by Netzsch STA 449 F3 was used to determine a suitable range for sintering temperature. The powder samples were heated at a rate of 5 °C/min in an inert environment with a constant argon gas flow of 50 mL/min from ambient temperature to 700 °C. This test was repeated three times to ensure the reproducibility of DSC results. Simulation software (JMatPro®) was used for thermodynamic calculations. The sintering of green objects was performed in a tube furnace with constant argon flow at a heating rate of 10 °C/min from an ambient temperature to the predetermined sintering temperatures of 530 °C, 545 °C, 560 °C, and 575 °C. Green objects were held at a sintering temperature for 5 h, followed by cooling in the furnace to room temperature. To study the impact of sintering time, some green objects were sintered at an isothermal condition of 530 °C for 50 h.

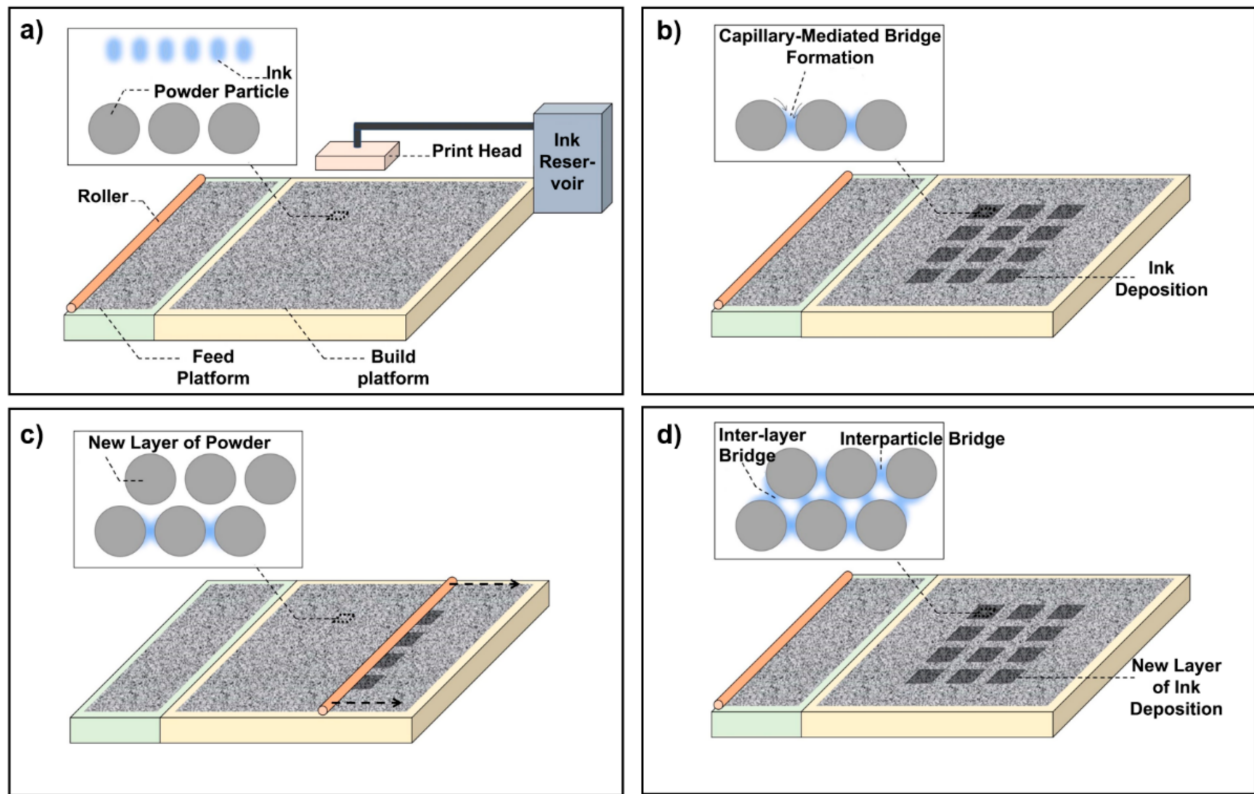


Figure 2. The capillary-mediated binderless AM process involves the following steps: (a) deposition of the ink onto the uppermost layer of AZ91 powder, (b) creation of a capillary-mediated liquid bridge within the interparticle gaps and their gradual transition into solid bridges, (c) dispensation of the ink in the desired area after the delivery and spreading of a new layer of powder on top of the previous one, and (d) formation of liquid bridges within the new layer as well as the preceding layer.

2.4. Characterization Methods

The carbon, oxygen, and hydrogen contents of the as-received AZ91 powder and the printed green samples were assessed using combustion-infrared absorbance (Eltra CS 800 Carbon/Sulfur Analyzer) and inert gas fusion-thermal conductivity (Eltra ONH 2000 Oxygen/Nitrogen/Hydrogen Analyzers), respectively. The test specimens were tested a minimum of two times to guarantee accuracy. The cross-sectional microstructure of green and sintered samples was examined using a scanning electron microscope (SEM, JEOL JSM-5600LV). The density of the green samples printed with different SLs was calculated by taking the mass of the printed cube (of sides 15 mm) over its volume, which was measured with a Vernier caliper. The density was measured for six cubes at each SL. The relative density of the sintered samples can be calculated using Archimedes' principle, as presented in Equation (1). This equation correlates the dry mass of the specimen (W_{dry}), the density of the liquid medium used (ρ_l), a mass of sample suspended in the liquid medium until all pore spaces fill with the liquid ($W_{\text{saturated}}$), a mass of saturated sample suspended in the liquid medium ($W_{\text{suspended}}$), and the bulk density of powder measured through a gas pycnometer (ρ_{Mg}). An oil-based medium was used to fill the pores because of the potential reactions of Mg samples in the presence of water. At least three test specimens were tested to ensure consistency and accuracy.

$$\text{Relative density} = \frac{(W_{\text{dry}} \times \rho_l)}{(W_{\text{saturated}} - W_{\text{suspended}}) \rho_{\text{Mg}}} \times 100 \quad (1)$$

3. Results and Discussion

3.1. Binder Jetting of Green AZ91D Objects

3.1.1. Determination of an Ink Saturation Level and Its Effect on Dimensional Accuracy

The deposited ink facilitates the formation of solid interparticle bridges through capillary bridging and determines the strength and dimensional accuracy of the printed green parts. However, the excessive deposition of the ink is undesirable due to the Mg powders' high affinity for oxygen [15]. Excess binder can result in the overgrowth of an outer oxide film covering each Mg particle. This excessively thick oxide layer will negatively influence the subsequent sintering step. This means that optimizing the amount of ink deposition, or saturation level, is paramount. A foundation of the capillary-mediated binderless 3D printing, which was developed using pure Mg and Mg-Zn-Zr powder, can be utilized to facilitate the fabrication of green parts [12,13]. Sufficient ink deposition on the print bed is required to form liquid or capillary bridges in accordance with the hysteretic nature of capillary bridging between neighboring powder particles, which is fundamental to establishing connections between adjacent powder particles. The minimal amount of ink needed to meet the hysteretic criterion for a powder bed composed of identical spherical particles at density ρ can be estimated with the following equation [12]:

$$SL = \frac{3\rho}{(1-\rho)} \left[\left(\frac{\rho_m}{\rho} \right)^{1/3} - 1 \right] + \frac{W_0}{(1-\rho)} \quad (\rho \leq \rho_m) \quad (2)$$

where SL is the ink saturation level, ρ_m is the maximum packing density of a given powder bed, and W_0 is the minimum amount of ink required for the formation of liquid capillary when the packing density is at the maximum (ρ_m). From both experimental and simulation studies [19,20], the value of W_0 can be estimated to be within the range of 3×10^{-4} to 2.4×10^{-2} . Powder tap density, as the tightest configuration of a free-flowing pile of powder, can be used as the maximum packing density (ρ_m). Similarly, powder packing density (ρ) can be assumed to be the apparent density of the powder, since virtually no compaction force applies while powder is being spread over the powder bed.

Considering these density values for the AZ91 powder and taking the upper bound of W_0 (i.e., 2.4×10^{-2}), the SL can be estimated to be 29.3%. This SL value is the minimal possible ink content that allows for the 3D assembly of AZ91 powder by capillary-mediated bridging. Figure 3a displays an as-printed green AZ91D cuboid fabricated with a 70% SL. As shown in Figure 3b, solid interparticle bridges formed from superficial interactions between the powder and ink enable 3D assembly of the AZ91 powder in the form of green objects. The 3D printing with a minimum SL of 30% was possible, but severe layer displacements during the build cycle negatively impacted the printing process due to the lack of ink penetration into preceding layers. In binder jetting, to facilitate the powder feedstock flow, each powder layer's thickness should be approximately three times the average particle size [21]. An insufficient penetration of ink across each powder layer occurred at a low SL. This led to layer displacements during powder spreading due to the shearing force exerted by the roller. This means that an ink SL level greater than the theoretically calculated SL of 29.3% will be needed to ensure sufficient ink penetration across each powder layer. Lateral and vertical permeations of the ink are necessary to form the solid capillary bridges between the interlayer particles and the particles of previous layers, providing as-printed objects with adequate strength and mechanical integrity. Although the layer displacement issue that was prevalent when printing with an SL of 30% was resolved by increasing the SL to 45%, the delamination and breakage of green objects when trying to remove the excess powder after its extraction from the powder bed became prevalent.

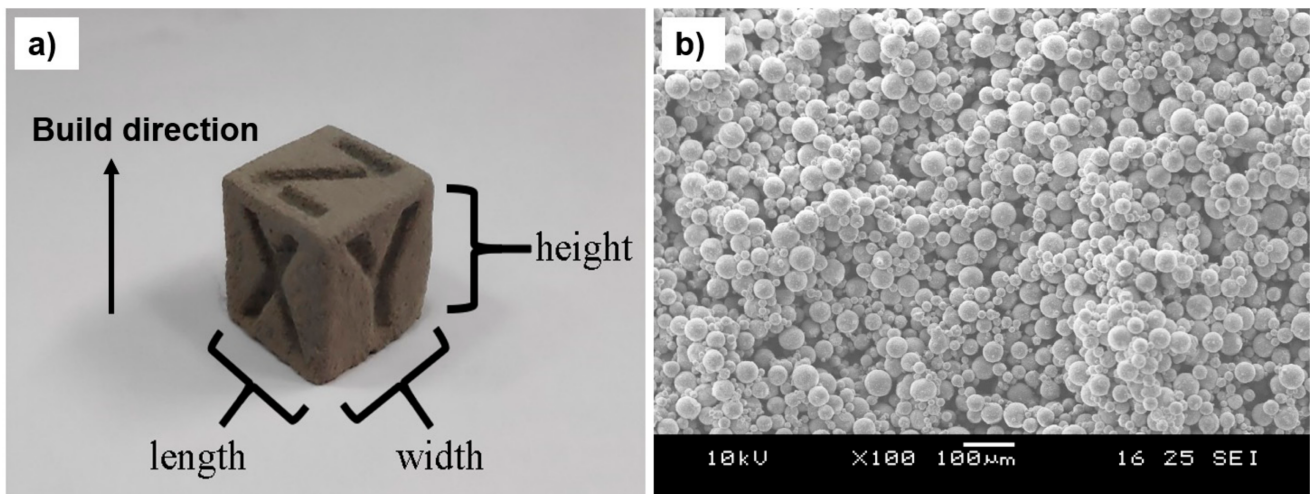


Figure 3. As-printed green AZ91D powder additively manufactured via capillary-mediated binderless printing with an SL of 70%. (a) A macrograph of a cube with imprints and (b) an SEM image showing the formation of solid interparticle bridges from the interaction between ink and powder.

Table 1 shows the actual dimension of cubes with sides 15 mm printed with four SLs of 70%, 90%, 110%, and 130%. For the cube printed with a 70% SL, rounded edges and rough surface textures were observed (Figure 3a). The dimensional accuracy of the green sample was unable to be maintained due to erosion during depowdering. As expected, the actual sizes of as-printed green cubes in all three dimensions constantly increased with increasing SL. Excess ink leaked from selectively deposited areas and led to undesirable lateral penetration. Furthermore, the vertical spreading of extra ink in an upper 2D layer permeated the layers below. These vertical and lateral permeations of excess ink caused dimensional errors and warping in the cube printed with a 130% SL.

Table 1. Actual sizes for as-printed green cuboids of dimension 15 mm × 15 mm × 15 mm printed with variations in SL.

Saturation Level (%)	Length (mm)	Width (mm)	Height (mm)
70	14.73 ± 0.21	14.88 ± 0.22	14.40 ± 0.29
90	15.09 ± 0.16	15.12 ± 0.11	15.14 ± 0.04
110	15.28 ± 0.08	15.43 ± 0.20	15.09 ± 0.13
130	15.46 ± 0.14	15.47 ± 0.26	15.18 ± 0.10

Interestingly, Table 1 shows that the dimension along the build direction (i.e., height) is smaller than the other two directions (i.e., length and width). Based on the permeation characteristics of ink droplets after being deposited by a print head onto a stationary powder bed, the droplets tend to permeate more laterally than vertically [22–24]. Therefore, an optimal adjustment of the SL to provide adequate lateral and vertical spreading of ink is essential for the stability of the printing build process, dimensional accuracy, and the isotropy of as-printed objects. We took the following measure to tackle the difference in the vertical and lateral permeation of the ink during the printing process. A suitable amount of ink was dispensed onto each layer of AZ91 powder to uphold the condition for successful capillary bridge formations in both inter- and intralayer, followed by spreading a subsequent layer of powder. Considering the calculated minimal ink threshold, the residual amount of ink in the preceding layer was removed prior to the ink deposition onto the succeeding layer. Such interplays between lateral and vertical spreading seemed to happen in the cubes printed with 90% and 110% SLs. In addition to tackling the ink spreading issue, using this measure during the build process addressed the dilemma of the ink saturation

level, the Mg powder-ink interaction, and the overall compositional change, all of which are discussed in Section 3.1.2.

3.1.2. Influence of Ink Saturation Levels on Interactions with AZ91 Powder

Figure 4 shows the SEM of green objects printed with SLs of 70%, 90%, and 110%. Based on the principle of capillary-mediated binderless 3D printing (Section 2.2), liquid bridges formed instantaneously within the interparticle space of the AZ91 powder layer. In addition, the liquid layer deposited onto the immediate surface of powder particles, away from the interparticle areas, was gradually transported into the interparticle regions. This flow process ended when the liquid on the surface of adjacent particles was either drained or disrupted. Meanwhile, interactions between the ink and the superficial layer of AZ91 powder were triggered within the interparticle regions and the surfaces of the particles. Hence, solid interparticle bridges evolved from the interactions between the AZ91 powder and ink within the bridge regions, as well as the transport of the products of interactions from the liquid layer away from the interparticle areas. Localizing the products from the ink's interactions with the AZ91 powder mainly occurred around the interparticle necks, which contributed to the formation of solid interparticle bridges. However, when the liquid layer on the particle surfaces was disrupted, the remaining ink adhered to the surface reacted with the AZ91 powder, leaving some nodules behind. These solid interparticle bridges, nodules, and unreacted regions on the surface of AZ91 powder in as-printed objects are indicated by each of the three arrows in Figure 4b.

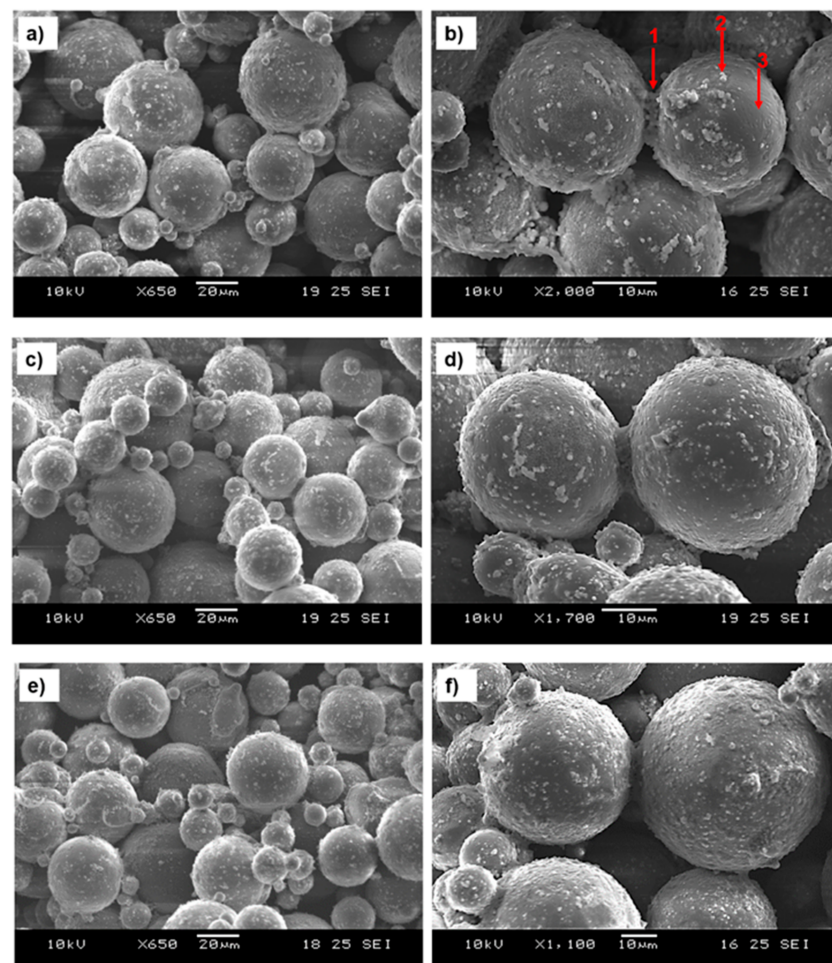


Figure 4. SEM images of the green AZ91 objects printed with various SLs showing the capillary-mediated solid interparticle bridges linking the AZ91 powder particles, (a,b) 70% SL, (c,d) 90% SL, and (e,f) 110% SL.

Comparing the SEM micrographs in Figure 4, especially Figure 4b,d,f, indicated that solid interparticle bridges did not wholly evolve in the green object printed with a 70% SL. In contrast, the bridges seemed to develop fully for the green object printed with 90% and 110% SLs. This observation is in line with the granular finish and erosion of the as-printed cube with an SL of 70% (Figure 3a), as discussed in Section 3.1.1. Comparisons of SEM micrographs also showed that an increase in SL increased the number of nodules formed on the surface of the particles and decreased the unreacted area. With the other printing parameters remaining constant, it can be concluded that the observed results were solely due to variations in the SL during printing. A higher SL released more ink onto the powder bed. This provided more reagents to react with the AZ91 powder and thus formed more interaction products in the resultant green objects. In essence, only ink–powder interaction in the interparticle bridge areas facilitated the 3D assembly of Mg powder into a green object. In other words, the formation of nodules is undesirable since it adversely affects the overall composition of green objects.

Basically, the SL during printing must be minimized to preserve the composition of AZ91 raw powder in an as-printed green object. Achieving this would be challenging, given the vital role of SL in the printability of AZ91 powder, as discussed in Section 3.1.1. Maintaining the chemical composition of Mg powder in binder jetting, especially the oxygen level, is paramount because of the high reactivity of Mg powder. Specifically, the native MgO film around the Mg powder grows in thickness with increasing oxidation. This worsens the sinterability of green Mg objects due to the substantial difference in melting points between Mg and MgO (i.e., 650 °C vs. 2850 °C). One can estimate the compositional changes occurring in the capillary-mediated printing by taking the ratio of the volume of interparticle bridges and the volume of the powder particles. This compositional change for identical spherical particles with a packing density (ρ) correlates with SL, as shown in the following equation [12].

$$V^* = SL \frac{(1 - \rho) \sin^2 \beta}{2\rho} \quad (3)$$

where V^* is the dimensionless bridge per powder particle and β is the average angle between adjacent interparticle bridges. As inferred from Equation (3), a higher SL increases the bridge-per-powder particle, leading to a higher compositional change. By taking 0.495 as the apparent density (ρ) measured for the AZ91 and β of 15°, the bridge-per-powder particle is approximated to be 6.3%, 19.4%, and 23.7% for SLs at 29.3%, 90%, and 110%, respectively.

Figure 5 displays the analysis of the C, H, and O levels in the AZ91 powder and the green objects printed at 90% and 110% SLs. The results showed a slight increase in C, H, and O contents in the green samples compared with the AZ91 powder. This compositional change is associated with interactions between the ink and the Mg powder, forming magnesium carbonate trihydrate, $MgCO_3 \cdot 3H_2O$, in the interparticle bridge areas and magnesium hydride and magnesium hydroxide on the surface of the powder particles, as thoroughly investigated for pure Mg and Mg-Zn-Zr powder in Refs. [13,15]. Elemental analyses of the objects with different SLs revealed that more compositional changes occurred in the object with a 110% SL. This is consistent with results from the SEM analyses (Figure 4), where more nodules formed on the surface of AZ91 powder printed with a 110% SL compared with a 90% SL. Comparisons of the chemical analysis results with the calculated bridge-per-powder particle showed the actual compositional change to be lower during the binderless printing of the AZ91 powder. This stemmed from the excess ink removal after forming liquid bridges, as described in Section 3.1.1, allowing for minimizing the ink content and its interaction with the Mg powder. Furthermore, the solid interparticle bridges (i.e., $MgCO_3 \cdot 3H_2O$) connecting the powder particles are highly porous, creating solid bridges while posing a minimal compositional change [12,13]. Finally, these interparticle bridges are determined to decompose to their primary constituents (i.e., MgO) during the subsequent sintering step of as-printed Mg objects, resulting in zero compositional change [12,13].

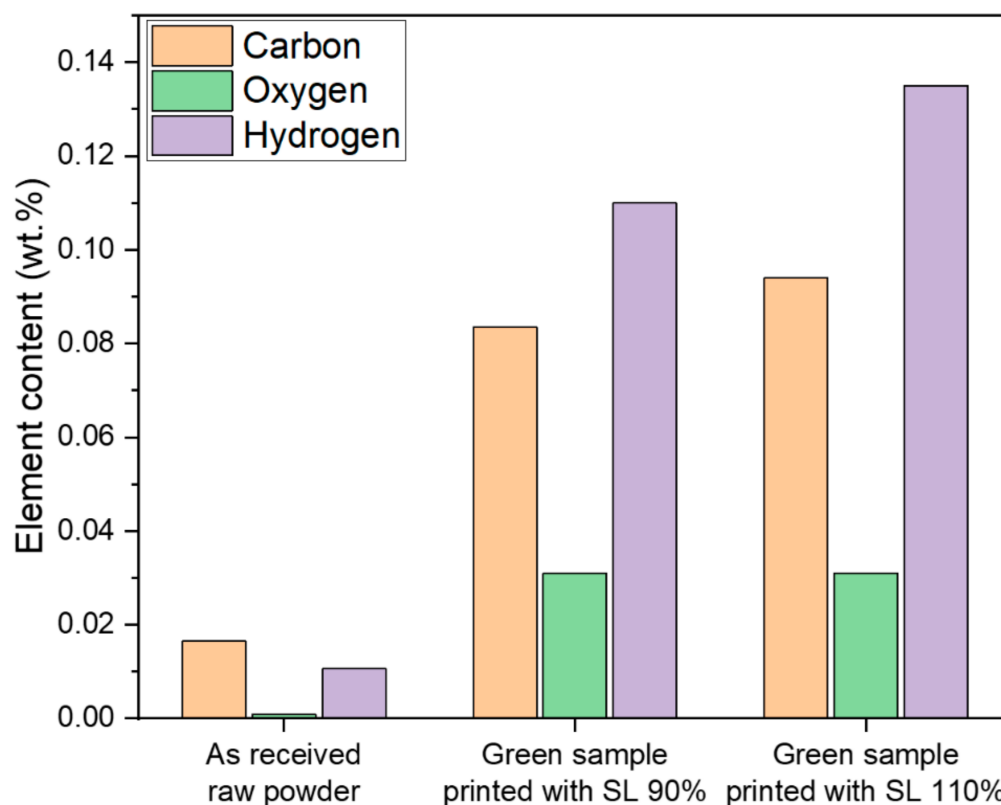


Figure 5. Elemental analyses of carbon, oxygen, and hydrogen in the as-received AZ91 powder and the green objects printed at 90% and 110% SLs.

3.2. Sintering of Green AZ91D Objects

With high geometrical precision and minimal alteration to the chemical composition of the green samples, the green objects printed with 90% SL were used to investigate the influence of sintering parameters on the sinterability of green samples. The densification of as-printed Mg objects remains a significant hurdle during the sinter-based AM of Mg alloys [4]. In binder jetting, several factors govern the sintering densification, which can be classified as follows [21]:

- (1) Characteristics of raw powder: elemental composition, particle size and distribution, morphology, flowability, and impurity concentration, especially with respect to oxygen content.
- (2) Binder jetting process parameters: powder–ink interactions, layer thickness, ink saturation level, and density of as-printed green samples.
- (3) Sintering profiles: residue, sintering furnace, temperature, duration, and atmospheres.

With the proper selection of binder jetting parameters (Section 3.1), we ensured that the surfaces of the AZ91 powder particles remained intact as much as possible. However, the presence of native MgO film on the external surface of individual Mg powder in an as-printed green object wholly retarded its solid-state sintering, given that the outer MgO layer was nearly impermeable to the diffusion of Mg atoms [15]. Due to the high thermal stability of MgO even above the boiling point of Mg (~1091 °C), it is essential to disrupt this oxide shell, either through physical breakage or reduction, before a feasible diffusional route for Mg atoms and sintering kinetics can be established. The deployment of liquid phase sintering was used to disrupt the surface oxide film and densify as-printed Mg objects produced by binder jetting and material extrusion [9,13,15,25].

3.2.1. Determination of Sintering Temperature Range

Thermal analysis was performed on the AZ91 powder to identify a suitable temperature range for super-solidus liquid phase sintering (LPS). Figure 6a shows the result for the

differential scanning calorimetry (DSC) of the AZ91 powder, with the solidus and liquidus temperatures of the powder sample determined to be ~ 500.8 °C and ~ 595.8 °C, respectively. Figure 6b displays the temperature dependence of the liquid fraction for AZ91 alloy having a similar chemical composition to the AZ91D powder, which is obtained from thermodynamic software. A good agreement was observed in terms of the liquidus temperature between the experimentally determined result and the thermodynamically calculated one (i.e., 602.5 °C). In contrast, a significant deviation of the solidus temperature from the DSC result (~ 500.8 °C) with the corresponding temperature from the thermodynamic calculation (~ 420 °C) was observed. This discrepancy can be attributed to the difference in sample morphology, with the thermodynamic calculation determined from the parameters of bulk AZ91, while, experimentally, the thermal analysis was conducted on AZ91 powder covered by a native MgO layer. Furthermore, the heating rate dependence of the thermal analysis results was recognized, with the increase in the heating rate during thermal analysis known to shift the onset of the phase transformation to a higher temperature [26]. Similarly, phase transformations obtained from thermodynamic calculations can vary with thermodynamic conditions/models. Combining the experimentally and theoretically obtained results, the sintering temperature window of 530 °C to 575 °C was chosen, providing a wide fraction of liquid phase up to 54.5 vol. %.

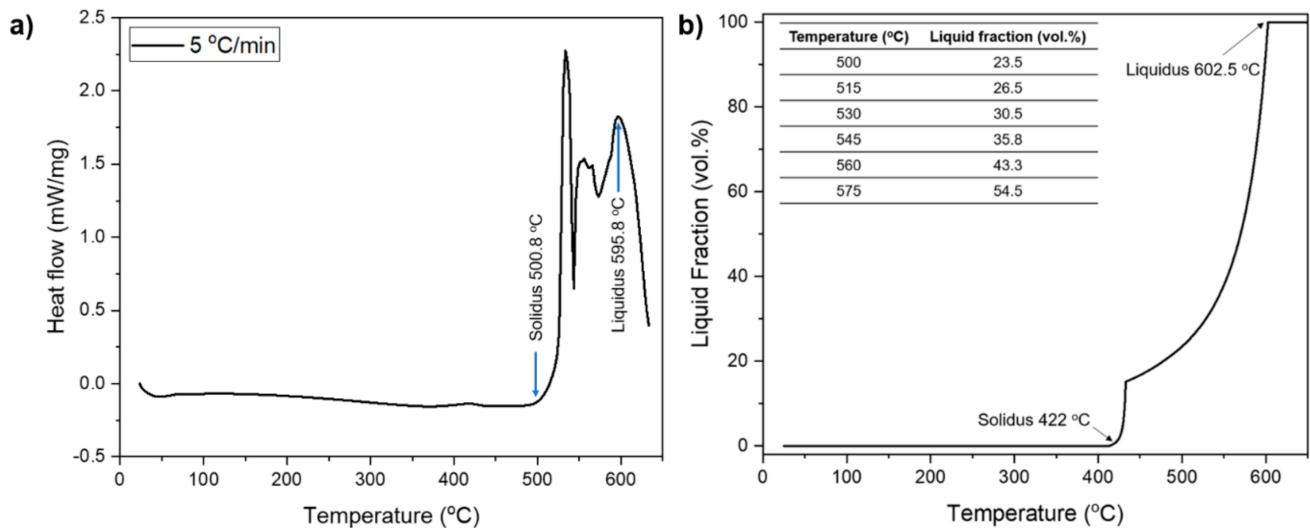


Figure 6. Thermal analysis of AZ91 alloy, (a) DSC of as-received powder at 5 °C/min, (b) temperature dependence of liquid fraction for Mg- 8.79 wt. % Al- 0.46 wt. % Zn- 0.17 wt. % Mn- 0.05 wt. % Si alloy determined by thermodynamic software.

3.2.2. Influence of Sintering Temperatures on Microstructure

Figure 7 shows the SEM images of as-printed AZ91 samples sintered at temperatures of 530 °C, 545 °C, 560 °C, and 575 °C, showing the impact of sintering temperatures on the sinter neck evolution. Sinter neck growth did not occur at a sintering temperature of 530 °C. Increasing the sintering temperature increased the diameter of the sinter necks and in turn shrunk the AZ91 powder particles. According to the mechanisms for super-solidus LPS [27], when the sintering temperature is above the solidus temperature, the liquid phase forms along the grain boundaries and within the grains of powder particles. Initially, the liquid phase was held inside each AZ91 particle due to the presence of the MgO film. With rising sintering temperatures, more liquid pockets formed inside each particle, increasing its internal pressure until the MgO film ruptured. This breakage turned as-printed objects into a liquid phase and a solid matrix of Mg powder particles, where an accelerated diffusion of Mg atoms occurred in the presence of a liquid phase [15]. Figure 8a shows the temperature dependence of total diffusivity for the AZ91 powder (i.e., the combined diffusivities of the Mg atoms existing in liquid and solid phases). As expected, forming a higher amount of liquid phase while increasing sintering temperature resulted in a remarkable increase in

the diffusion rate, with a 15× increase in total diffusivity when the temperature increased from 530 °C to 575 °C.

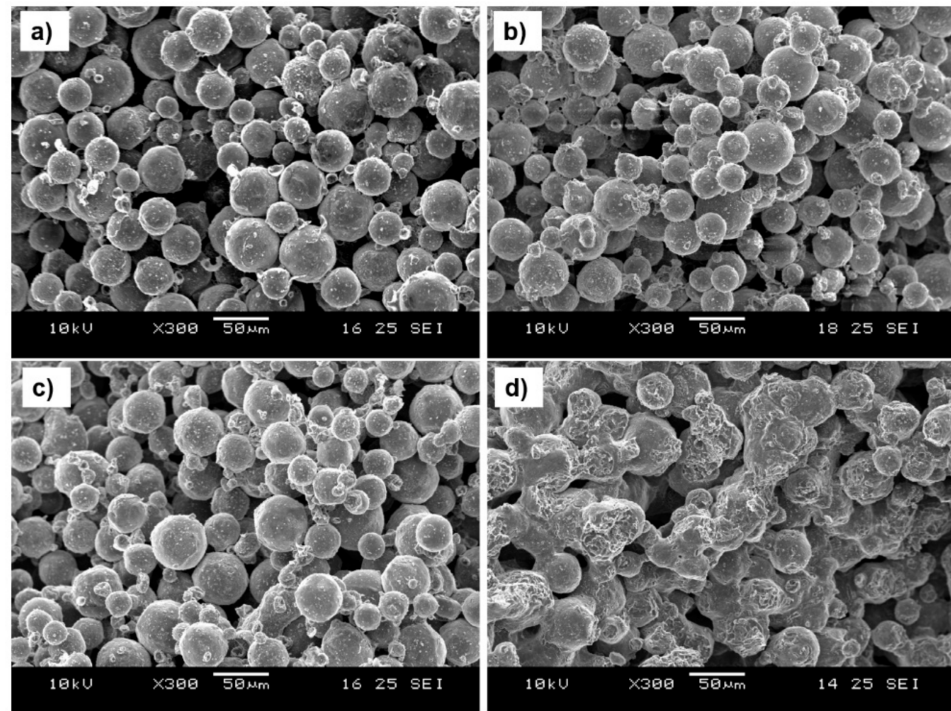


Figure 7. SEM images of as-printed objects after sintering for 5 h at different temperatures. (a) 530 °C, (b) 545 °C, (c) 560 °C, and (d) 575 °C.

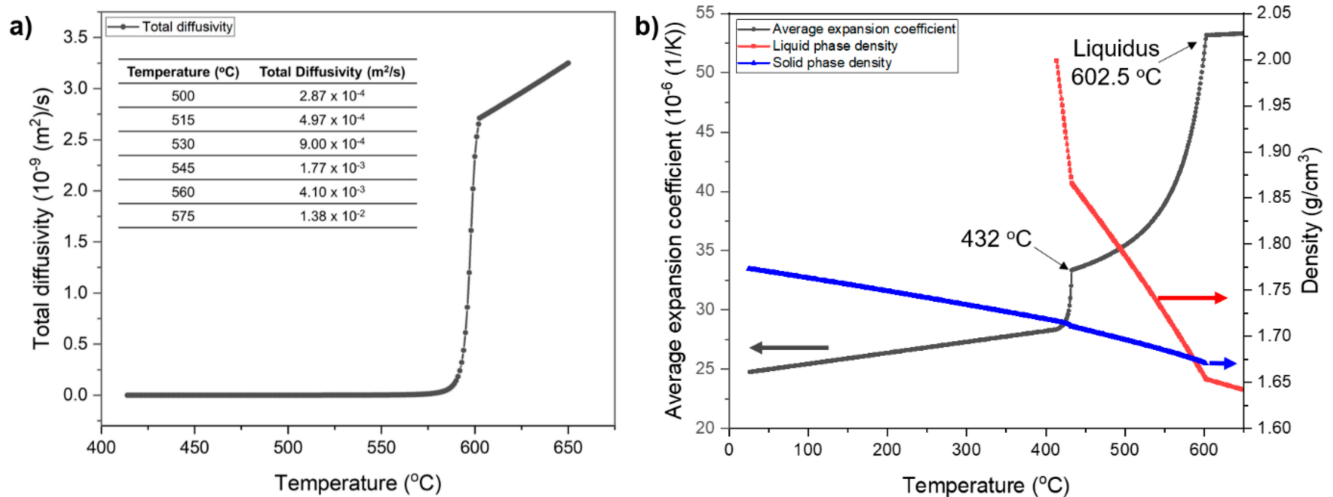


Figure 8. Temperature dependence of Mg-8.79 wt. % Al-0.46 wt. % Zn-0.17 wt. % Mn-0.05 wt. % Si calculated by thermodynamic software. (a) Total diffusivity coefficient and (b) density and average expansion coefficient.

3.2.3. Influence of Sintering Temperatures on Macrostructure

Figure 9 shows pictorial representations of the objects with different sizes and geometries after sintering at various temperatures for 5 h. The seeping of the liquid phase to the surface of the sintered AZ91 samples was observed at a sintering temperature of 545 °C, forming a series of small spheres. When the sintering temperature increased to 560 °C and 575 °C, more liquid phases were exuded, more prominent blisters were raised, and swelling occurred, leading to more shape loss. As seen in Figure 8b, the liquid phase formation during LPS resulted in volume expansion, since the liquid phase density was rapidly

decreasing. This caused a remarkable increase in the coefficient of average expansion with rising temperature/liquid fraction (Figure 8b). In addition to the high surface tension of the molten Mg phase, the wettability of MgO by molten Mg droplets is poor [28]. In LPS, the capillary force pulled the liquid phase into the sinter neck areas. When the amount of liquid phase exceeded the capacity of the capillary pressure to stay within the sinter necks, the surplus liquid was drawn out to the outer surface of the Mg objects and caused the swelling effect [15]. Swelling during sintering was reported for binder jet-printed ZK60 powder and material extrusion-printed pure Mg alloy [13,15,25]. Swelling led to dimensional loss and chemical compositional degradation of the sintered samples.

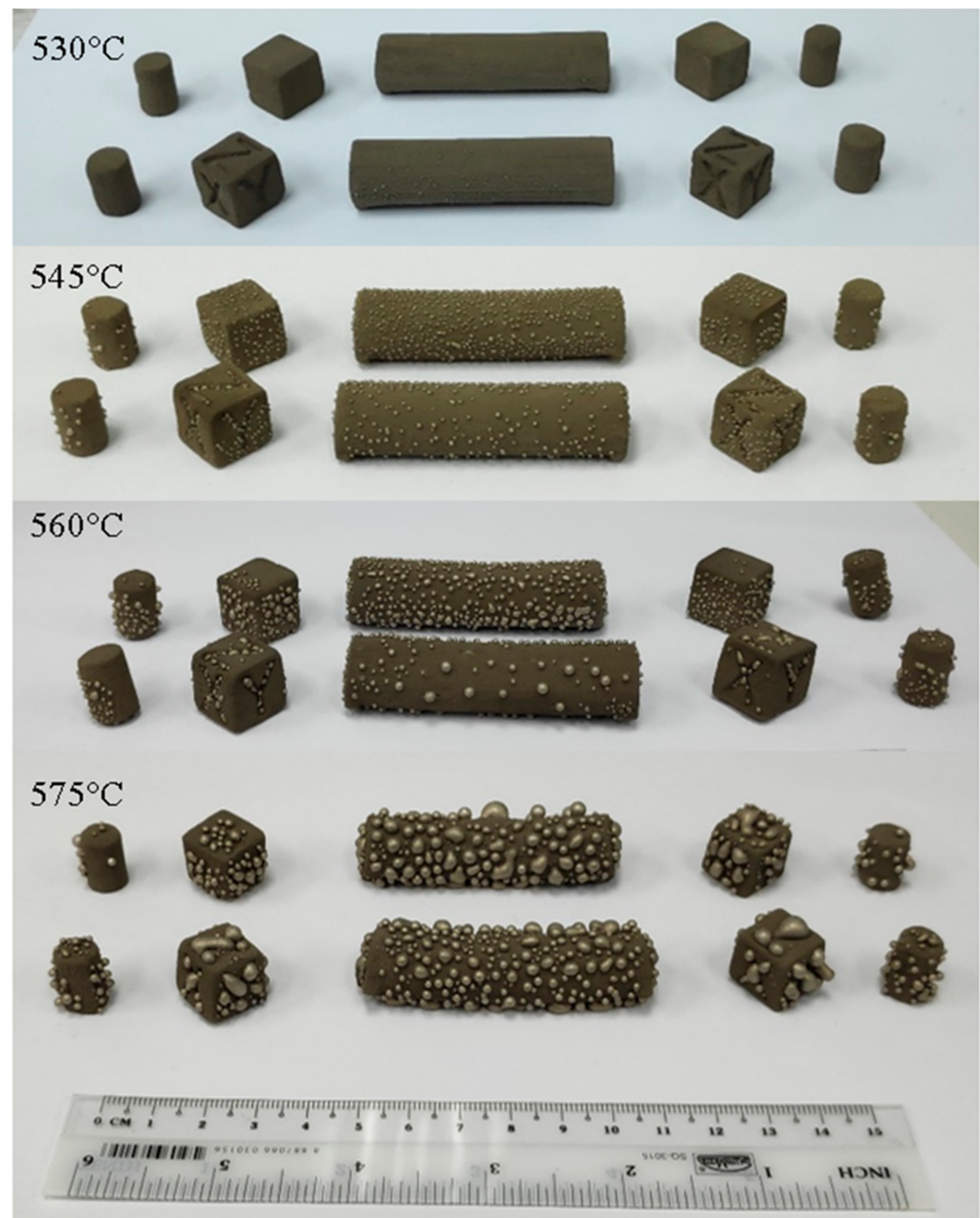


Figure 9. Macrographs of as-printed objects with different sizes and geometries after sintering at various temperatures for 5 h.

Determining the optimal fraction of the liquid phase during LPS is challenging. While an increase in a liquid phase fraction (at a higher sintering temperature) enhanced the densification rate during LPS, more liquid led to a lower skeletal stability of the objects, a

tendency for distortion, a loss of dimensional accuracy, and susceptibility to swelling. As a two-step AM method, the dimension accuracy of binder jet-printed components is highly dependent on the densification step. As such, an ideal sintering process should result in only the isotropic shrinkage of green objects. Given Figures 8b and 9, the optimum liquid volume fraction at which swelling did not occur was in the range of ~30 vol. % to ~35 vol. %. The literature on the LPS of powder metallurgy compacts revealed that the optimal content for the liquid phase was between 20 vol. % and 40 vol. % [27]. The optimum liquid fractions during the sintering of binder jet-printed green ZK60 Mg powder in an electrical-resistance furnace and microwave furnace were determined to be ~24 vol. % [15] and ~11 vol. % [14], respectively. In contrast, Su et al. [9] used a two-step sintering profile for complete liquid phase sintering of a binder jet-printed AZ91D sample, where as-printed samples were rapidly quenched to 600 °C and held for 6 h after an initial heating phase of 700 °C for 30 min. Using this sintering profile, a density level greater than 99% was achieved in a small cylindrical sample. Nevertheless, comprehensive studies are required to investigate whether and how this complete liquid phase method may be applied to sinter larger green components with more complex geometries.

3.2.4. Influence of Sintering Temperatures on Density

Table 2 shows the Archimedes' density results of the AZ91 objects sintered at different temperatures. Compared with the density of as-printed objects, the density values increased slightly with increasing sintering temperatures. This contrasts with the observations from the SEM analyses of increased sinter neck diameters in the AZ91 particles (Section 3.2.2). The reason for this discrepancy between the density results and the SEM observation is as follows. Shrinkage refers to a decrease in dimensions, while swelling refers to an increase in size. From a microscopic standpoint, particles shrink for two reasons: (1) disintegration into solid and liquid phases and (2) consolidation due to the growth of sinter neck diameters, as supported by SEM images (Figure 7). From a macroscopic viewpoint, swelling causes blisters on the surface of objects, increasing the objects' overall volume. Hence, this macroscopic swelling tends to decrease the objects' density, as opposed to the shrinkage tendency occurring at the microscopic scale. An interplay between these two opposing effects determines the object density measured by Archimedes' principle.

Table 2. Density of the AZ91 powder in various conditions (as-received, as-printed, and as-sintered).

Specimen Condition	Density (g/cm ³)	Relative Density (%) $\frac{\text{Density}}{\text{Pycnometer density}} \times 100$
Pycnometer density of AZ91 powder	1.8872 ± 0.0009	100
Apparent density of AZ91 powder	0.9413 ± 0.0833	49.9
Tap density of AZ91 powder	1.195 ± 0.016	63.3
Pycnometer density of as-printed green object	2.0277 ± 0.0009	100
As-printed green object	1.0108 ± 0.0241	49.8
As-printed green object after sintering at 530 °C for 5 h	0.969 ± 0.007	51.3
As-printed green object after sintering at 545 °C for 5 h	1.000 ± 0.007	53.0
As-printed green object after sintering at 560 °C for 5 h	1.005 ± 0.005	53.3
As-printed green object after sintering at 575 °C for 5 h	1.036 ± 0.023	54.9
As-printed green object after sintering at 530 °C for 50 h	1.030 ± 0.005	54.6

From Table 2, the relative density of green objects was 49.8%, which is equal to the apparent density of the starting Mg powder (i.e., 49.9%). In view of the insignificant compression of a powder bed by a counter-rotating roller with each spread of a new powder layer over the powder bed areas, only gravity force influenced the powder compaction [21]. As such, the packing density of a green sample would be lower than the tap density of its constituent powder. Interestingly, when comparisons were made between the relative density of sintered samples and the tap density of the starting AZ91 powder, a lower relative density in the sintered samples implied that the powder packing state in all sintered objects did not come close to that of the tapped powder, which was the tightest packing configuration for the free-flowing powder. Capillary stress is the main driving force for the LPS process, such that a higher capillary pressure results in greater densification [29]. Increasing the sintering temperature from 530 °C to 575 °C increased the nominal liquid fraction during the sintering of as-printed AZ91 objects from 30.5 vol. % to 54.5 vol. %. However, the actual liquid content in the sinter neck regions at a higher sintering temperature remained the same (i.e., 30.5 vol.% to 35.8 vol. %) due to the swelling effect. In other words, such a nominal increment of liquid fractions did not affect the sintering driving force, and thus the sintering densification rates, because the excess liquid fraction was drawn out from the sinter neck areas. In view of this hypothesis, the marginal improvement in density observed with increasing sintering temperatures was mainly associated with enhancing the total diffusivity values with temperatures, as discussed in Section 3.2.2.

We hypothesized that the root cause of the marginal change in density with increasing sintering temperatures lies in the characteristics of the raw AZ91 powder. Drawing an analogy between the results obtained in this study and those reported in the literature could shed some light on the determining factors. In our previous study [15] on LPS of binder jet-printed ZK60 powder, the green sample had a relative density of 55%. Three densification zones during sintering were identified based on the density change rate as a function of the liquid volume fraction. In the first zone with liquid fraction <20 vol. %, the density of ZK60 samples sintered for 5 h was lower than that of the powder's tap density (i.e., 58.5%). In the second zone, where the liquid fraction ranged from 20 vol. % to 24.4 vol. %, the density of ZK60 samples sintered for 5 h surpassed the powder's tap density. In the third zone, where the liquid fraction was between 24.4 vol. % and 43.7 vol. %, the density showed an increasing trend and reached a maximum of 69.3%. However, the swelling effect caused the densification rate to decrease compared with the second region. The liquid fractions at which swelling occurred for the AZ91D and ZK60 powders were within the same range. In particular, swelling occurred at liquid fractions >24 vol. % and >30.5 vol. % for the ZK60 powder [15] and the AZ91 powder, respectively. This similarity implied that the liquid content and swelling phenomenon appeared to not be the most critical factor in lowering the densification rates of the AZ91 powder. All process parameters used in the present work were similar to our previous study, except for the powder packing density [15].

The packing density of as-printed parts, governing the coordination number of particles during the sintering process, is another crucial factor in determining the densification rate. As mentioned above, an analogy between the current study results with the one reported for ZK60 powder could provide insight into the impact of powder packing density on the sintering densification rate of binder jet-printed Mg powder. In this regard, the ratio of as-printed green density to the tap density of raw powder gives an informative dimensionless number for the sake of comparison. The ratio in the present study was ~79%, whereas the ratio in our previous work on ZK60 powder was ~94%. Liu et al. found that the capillary force in LPS diminishes when the distance between neighborhood particles increases [30]. Accordingly, in the as-printed AZ91 object with a packing density similar to the configuration of its free-flowing powder condition, the sintering driving force is smaller when compared with the ZK60 counterparts. Moreover, adjacent Mg particles must be connected by forming liquid contents to effectively consolidate during super-solidus LPS. With a lower packing density, the average separation between the adjacent powder

particle increases, reducing the probability of an effective liquid bridge forming between them, especially in the presence of a restricted liquid phase content. As discussed above, increasing the sintering temperature did not impact the sintering driving force because the actual liquid phase within the sinter neck bridges remained the same. Taken together, the combination of swelling and the low packing density of green objects led to the low sintering densification rate observed in as-printed AZ91 powder.

3.2.5. Influence of Sintering Time on Density

Extending the sintering time is one way to densify green objects further. As listed in Table 2, with the extension of the isothermal dwell time at 530 °C from 5 h to 50 h, the sintered density increased from 51.3% to 54.6%. The extension of sintering time resulted in greater densification, although the density value was still much lower than the powder's tap density (i.e., 63.3%). Such low sintering kinetics and, in turn, density increment in response to the extension of sintering time, make the sintering process unfeasible, implying the vital role of powder packing density on the sinterability of as-printed green Mg objects. One possible avenue of future work is to develop Mg powder feedstock with superior sinterability by fine-tuning the powder particle size distribution or adding sintering aids.

4. Conclusions

A detailed perspective on fundamental concepts needed for developing capillary-mediated binderless 3D printing of AZ91D powder was outlined in a systematic manner. This understanding of process parameters and underlying principles can be applied to binder jetting and sintering of other materials, especially reactive metals. The present study has led to the following conclusions:

- (1) An ink saturation level higher than the minimum threshold value (i.e., 29.3% SL) was needed for the adequate vertical and lateral permeation of ink and the formation of fully evolved solid interparticle bridges between AZ91D particles. The green cubes printed with 90% and 110% SLs had great dimensional accuracy and mechanical integrity.
- (2) The dimensionless number of bridges per powder particle and the results of elemental analyses demonstrated that a lower ink saturation level minimized the compositional change in as-printed AZ91 objects. The green objects printed with a 90% SL showed a marginal compositional shift in O, H, and C compared with the raw AZ91D powder.
- (3) Increasing the sintering temperature from 530 °C to 575 °C increased the nominal liquid fraction during the sintering of as-printed AZ91 objects from 30.5 vol. % to 54.5 vol. %. Because the swelling occurred at temperatures >545 °C, the actual liquid content in the sinter neck regions at a higher sintering temperature remained the same (i.e., 30.5 vol. % to 35.8 vol. %).
- (4) With increasing sintering temperatures and time, the density of as-sintered samples increased slightly compared with those of the as-printed condition (i.e., 1.5% to 5.1%).
- (5) The sintering densification rate of binder jet-printed Mg powder was governed by the swelling phenomenon and the packing density of as-printed green objects.

Author Contributions: Conceptualization, M.S.; methodology, M.S. and M.L.S.N.; validation, M.S., J.H.H., S.X.Z. and H.L.S.; formal analysis, M.S. and K.X.K.; investigation, M.S. and J.H.H.; resources, S.X.Z.; data curation, K.X.K., J.H.H. and M.S.; writing—original draft preparation, M.S. and K.X.K.; writing—review and editing, M.S.; supervision, M.L.S.N.; project administration, H.L.S.; funding acquisition, M.L.S.N. All authors have read and agreed to the published version of the manuscript.

Funding: This research was funded by the first Singapore–Germany academic–industry (2 + 2) international collaboration grant (Grant no. A1890b0050).

Data Availability Statement: The data presented in this study are available on request from the corresponding authors. The data are not publicly available due to ongoing studies.

Acknowledgments: Jia Hern Ho would like to thank Chou Siaw Meng from the School of Mechanical and Aerospace Engineering (MAE) of Nanyang Technological University (NTU), Singapore, for his support and guidance.

Conflicts of Interest: The authors declare no conflict of interest.

References

1. Gusieva, K.; Davies, C.H.J.; Scully, J.R.; Birbilis, N. Corrosion of magnesium alloys: The role of alloying. *Int. Mater. Rev.* **2015**, *60*, 169–194. [[CrossRef](#)]
2. Weiler, J.P. Exploring the concept of castability in magnesium die-casting alloys. *J. Magnes. Alloys* **2021**, *9*, 102–111. [[CrossRef](#)]
3. Ezhilmaran, V.; Suya Prem Anand, P.; Kannan, S.; Sivashanmugam, N.; Jayakrishna, K.; Kalusuraman, G. Review of bioresorbable AZ91, AZ31 and Mg–Zn–Ca implants and their manufacturing methods. *Mater. Sci. Technol.* **2022**, 1–25. [[CrossRef](#)]
4. Zeng, Z.; Salehi, M.; Kopp, A.; Xu, S.; Esmaily, M.; Birbilis, N. Recent progress and perspectives in additive manufacturing of magnesium alloys. *J. Magnes. Alloys* **2022**, *10*, 1511–1541. [[CrossRef](#)]
5. Schmid, D.; Renza, J.; Zaeh, M.F.; Glasschroeder, J. Process Influences on Laser-beam Melting of the Magnesium Alloy AZ91. *Phys. Procedia* **2016**, *83*, 927–936. [[CrossRef](#)]
6. Li, X.; Fang, X.; Wang, S.; Wang, S.; Zha, M.; Huang, K. Selective laser melted AZ91D magnesium alloy with superior balance of strength and ductility. *J. Magnes. Alloys* **2022**. [[CrossRef](#)]
7. Bi, J.; Shen, J.; Hu, S.; Zhen, Y.; Yin, F.; Bu, X. Microstructure and mechanical properties of AZ91 Mg alloy fabricated by cold metal transfer additive manufacturing. *Mater. Lett.* **2020**, *276*, 128185. [[CrossRef](#)]
8. Vishwanath, A.S.; Rane, K.; Schaper, J.; Strano, M.; Casati, R. Rapid production of AZ91 Mg alloy by extrusion based additive manufacturing process. *Powder Metall.* **2021**, *64*, 370–377. [[CrossRef](#)]
9. Su, C.; Wang, J.; Li, H.; You, Z.; Li, J. Binder-jetting additive manufacturing of Mg alloy densified by two-step sintering process. *J. Manuf. Process.* **2021**, *72*, 71–79. [[CrossRef](#)]
10. Mostafaei, A.; Elliott, A.; Barnes, J.; Li, F.; Tan, W.; Cramer, C.; Nandwana, P.; Chmielus, M. Binder jet 3D printing—Process parameters, materials, properties, modeling, and challenges. *Prog. Mater. Sci.* **2021**, *119*, 100707. [[CrossRef](#)]
11. Ziaee, M.; Crane, N. Binder jetting: A review of process, materials, and methods. *Addit. Manuf.* **2019**, *28*, 781–801. [[CrossRef](#)]
12. Salehi, M.; Maleksaeedi, S.; Nai, S.M.L.; Meenashisundaram, G.K.; Goh, M.H.; Gupta, M. A paradigm shift towards compositionally zero-sum binderless 3D printing of magnesium alloys via capillary-mediated bridging. *Acta Mater.* **2019**, *165*, 294–306. [[CrossRef](#)]
13. Salehi, M.; Maleksaeedi, S.; Nai, M.L.S.; Gupta, M. Towards additive manufacturing of magnesium alloys through integration of binderless 3D printing and rapid microwave sintering. *Addit. Manuf.* **2019**, *29*, 100790. [[CrossRef](#)]
14. Salehi, M.; Seet, H.L.; Gupta, M.; Farnoush, H.; Maleksaeedi, S.; Nai, M.L.S. Rapid densification of additive manufactured magnesium alloys via microwave sintering. *Addit. Manuf.* **2021**, *37*, 101655. [[CrossRef](#)]
15. Salehi, M.; Maleksaeedi, S.; Sapari, M.A.B.; Nai, M.L.S.; Meenashisundaram, G.K.; Gupta, M. Additive manufacturing of magnesium–zinc–zirconium (ZK) alloys via capillary-mediated binderless three-dimensional printing. *Mater. Des.* **2019**, *169*, 107683. [[CrossRef](#)]
16. Kuah, K.X.; Salehi, M.; Huang, Z.; Zhang, S.X.; Seet, H.L.; Nai, M.L.S.; Blackwood, D.J. Surface Modification with Phosphate and Hydroxyapatite of Porous Magnesium Scaffolds Fabricated by Binder Jet Additive Manufacturing. *Crystals* **2022**, *12*, 1850. [[CrossRef](#)]
17. Kuah, K.X.; Salehi, M.; Ong, W.K.; Seet, H.L.; Nai, M.L.S.; Wijesinghe, S.; Blackwood, D.J. Insights into the influence of oxide inclusions on corrosion performance of additive manufactured magnesium alloys. *npj Mater. Degrad.* **2022**, *6*, 36. [[CrossRef](#)]
18. Kuah, K.X.; Blackwood, D.J.; Ong, W.K.; Salehi, M.; Seet, H.L.; Nai, M.L.S.; Wijesinghe, S. Analysis of the corrosion performance of binder jet additive manufactured magnesium alloys for biomedical applications. *J. Magnes. Alloys* **2022**, *10*, 1296–1310. [[CrossRef](#)]
19. Scheel, M.; Seemann, R.; Brinkmann, M.; Di Michiel, M.; Sheppard, A.; Breidenbach, B.; Herminghaus, S. Morphological clues to wet granular pile stability. *Nat. Mater.* **2008**, *7*, 189. [[CrossRef](#)]
20. Kohonen, M.M.; Geromichalos, D.; Scheel, M.; Schier, C.; Herminghaus, S. On capillary bridges in wet granular materials. *Phys. A Stat. Mech. Its Appl.* **2004**, *339*, 7–15. [[CrossRef](#)]
21. Salehi, M.; Gupta, M.; Maleksaeedi, S.; Nai, M.L.S. *Inkjet Based 3D Additive Manufacturing of Metals*; Materials Research Forum LLC: Millersville, PA, USA, 2018.
22. Lu, K.; Hiser, M.; Wu, W. Effect of particle size on three dimensional printed mesh structures. *Powder Technol.* **2009**, *192*, 178–183. [[CrossRef](#)]
23. Zhou, Z.; Buchanan, F.; Mitchell, C.; Dunne, N. Printability of calcium phosphate: Calcium sulfate powders for the application of tissue engineered bone scaffolds using the 3D printing technique. *Mater. Sci. Eng. C* **2014**, *38*, 1–10. [[CrossRef](#)] [[PubMed](#)]
24. Miyanaji, H.; Zhang, S.; Lassell, A.; Zandinejad, A.; Yang, L. Process Development of Porcelain Ceramic Material with Binder Jetting Process for Dental Applications. *JOM* **2016**, *68*, 831–841. [[CrossRef](#)]
25. Dong, J.; Li, Y.; Lin, P.; Leeftang, M.A.; van Asperen, S.; Yu, K.; Tümer, N.; Norder, B.; Zadpoor, A.A.; Zhou, J. Solvent-cast 3D printing of magnesium scaffolds. *Acta Biomater.* **2020**, *114*, 497–514. [[CrossRef](#)]
26. Salehi, M.; Maleksaeedi, S.; Farnoush, H.; Nai, M.L.S.; Meenashisundaram, G.K.; Gupta, M. An investigation into interaction between magnesium powder and Ar gas: Implications for selective laser melting of magnesium. *Powder Technol.* **2018**, *333*, 252–261. [[CrossRef](#)]

27. German, R.M. *Sintering: From Empirical Observations to Scientific Principles*; Elsevier Science & Technology Books: Amsterdam, The Netherlands, 2014.
28. Fujii, H.; Izutani, S.; Matsumoto, T.; Kiguchi, S.; Nogi, K. Evaluation of unusual change in contact angle between MgO and molten magnesium. *Mater. Sci. Eng. A* **2006**, *417*, 99–103. [[CrossRef](#)]
29. Liu, Y.; Tandon, R.; German, R.M. Modeling of supersolidus liquid phase sintering: I. Capillary force. *Metall. Mater. Trans. A* **1995**, *26*, 2415–2422. [[CrossRef](#)]
30. Liu, J.; Cardamone, A.L.; German, R.M. Estimation of capillary pressure in liquid phase sintering. *Powder Metall.* **2001**, *44*, 317–324. [[CrossRef](#)]

Disclaimer/Publisher’s Note: The statements, opinions and data contained in all publications are solely those of the individual author(s) and contributor(s) and not of MDPI and/or the editor(s). MDPI and/or the editor(s) disclaim responsibility for any injury to people or property resulting from any ideas, methods, instructions or products referred to in the content.